nature communications

Article

https://doi.org/10.1038/s41467-024-51865-x

Energy-efficient dynamic 3D metasurfaces via spatiotemporal jamming interleaved assemblies for tactile interfaces

Received: 12 March 2024

Accepted: 19 August 2024

Published online: 26 August 2024

Check for updates

Siqi An[1,2,4], Xiaowen Li[1,2,4], Zengrong Guo[1,4], Yi Huang[1], Yanlin Zhang[1,2] & Hanqing Jiang[1,2,3]

Inspired by the natural shape-morphing abilities of biological organisms, we introduce a strategy for creating energy-efficient dynamic 3D metasurfaces through spatiotemporal jamming of interleaved assemblies. Our approach, diverging from traditional shape-morphing techniques reliant on continuous energy inputs, utilizes strategically jammed, paper-based interleaved assemblies. By rapidly altering their stiffness at various spatial points and temporal phases during the relaxation of the soft substrate through jamming, we enable the formation of refreshable, intricate 3D shapes with a desirable load-bearing capability. This process, which does not require ongoing energy consumption, ensures energy-efficient and lasting shape displays. Our theoretical model, linking buckling deformation to residual pre-strain, underpins the inverse design process for an array of interleaved assemblies, facilitating the creation of diverse 3D configurations. This metasurface holds notable potential for tactile displays, particularly for the visually impaired, heralding possibilities in visual impaired education, haptic feedback, and virtual/augmented reality applications.

The controlled transformation of two-dimensional (2D) matters into complex three-dimensional (3D) structures holds promise for various emerging areas, including soft robotics[1–3], biomedical devices[4,5], metamaterials[6,7], and the virtual reality/augmented reality applications[8,9]. A variety of methods have emerged to create complex 3D structures. These include the use of responsive materials that respond to external stimuli, such as liquid crystal elastomers[10–12], dielectric elastomers[13,14], swellable hydrogels[15–17], and magnetically responsive soft materials[18,19]. Other techniques involve origami/kirigami structures[20–24], soft pneumatic actuators[25–28], multi-material structures[29–31], and mechanical buckling of pre-patterned 2D strips on soft substrates[32–35]. These methods, however, generally preset shape-morphing rules at fabrication, thus the final 3D shapes are usually predetermined and cannot be refreshed. Efforts have been dedicated to enable reprogrammable 3D structures, such as thermally activated robotic surfaces[36], Lorentz force-driving mechanical metasurfaces[37], loading-path controlled mechanical assembly[38,39], with the cost of uninterrupted energy input[36,37,40–42] or with limited transformable 3D geometries[38,39,43–45]. Additionally, these reprogrammable shape-morphing structures generally lack an effective load-bearing capability[37], which restricts their practical applications in tactile devices given that a gentle touch may collapse the morphed structures.

In this paper, we introduce an approach for an energy-efficient, dynamically refreshable 3D metasurface consisting of units with tunable stiffness through spatiotemporally jamming interleaved assemblies on soft substrates. On a pre-stretched soft substrate, the interleaved assemblies can be individually addressed and spatially jammed by vacuum at distinct temporal instances during the relaxation of the pre-strain. Jamming the initially flat interleaved assemblies at different spatial locations creates a 2D array of interleaved

[1]School of Engineering, Westlake University, Hangzhou, Zhejiang 310030, China. [2]Westlake Institute for Advanced Study, Hangzhou, Zhejiang 310024, China. [3]Research Center for Industries of the Future, Westlake University, Hangzhou, Zhejiang 310030, China. [4]These authors contributed equally: Siqi An, Xiaowen Li, Zengrong Guo. e-mail: hanqing.jiang@westlake.edu.cn

assembles with different stiffness, which would buckle to 3D architectures with distinct profiles upon releasing the pre-stretched soft substrates in the temporal domain. Once jammed, the formed 3D shapes do not require constant energy input to maintain the shapes and exhibit a desirable load-bearing capability. The jammed units can also be subsequently unjammed to recover to the 2D shapes. Thus, the present approach can achieve dynamic refreshability and display the 3D shapes using an energetically efficient way. The formed 3D shapes are theoretically predictable depending on the geometries of the interleaved assemblies and the residual pre-strain; thus, inverse design can be applied to achieve desired 3D shapes. Attributed to the dynamic refreshability and load-bearing capability, complicated 3D architectures were demonstrated using a 32 × 24 array of interleaved assembly, which function as a tactile display for visually impaired or could be used as tactile metasurfaces in the virtual reality/augmented reality applications. This approach not only demonstrates a significant advancement in 3D shape morphing technologies but also holds promise for revolutionizing user interfaces and sensory experiences in numerous applications.

Results

Jamming of interleaved papers for tunable tensile rigidity and spatiotemporal buckling design strategy

Inspired by the well-known friction experiments of interleaved phone books[46], we designed a unit with tunable tensile rigidity. The unit consists of interleaved assemblies (i.e., papers) formed by interlacing two zigzag strips within an airtight elastomeric pocket with a tubular air duct (Fig. 1a and Methods). The stiffness, or tensile rigidity, of this assembly can be readily adjusted through a process known as jamming[47]. For example, the tensile rigidity of the unjammed elastomeric pocket (i.e., negative pressure $P = 0$) is 0.723 N/mm, which can increase to as high as 21.715 N/mm upon jamming (e.g., $P = 60$ kPa) for a 4-ply interleaved assembly. This represents an increase in rigidity of over 30 times (Fig. 1b, c). The correlation between tensile rigidity and applied negative pressure is detailed in Fig. 1c (see Supplementary Fig. 1 and Methods for details). This dual-domain tensile rigidity leads to three distinct scenarios: an OFF state representing low tensile rigidity without jamming ($P = 0$), a variable stiffness scenario with moderate tensile rigidity ($0 < P < P_{th}$), where P_{th} denotes the specific threshold negative pressure that varies depending on the ply count of the interleaved papers, and an ON state characterized by high and relatively constant tensile rigidity achieved through jamming ($P > P_{th}$).

When unjammed, the interleaved assemblies exhibit elasticity comparable to elastomeric materials. The maximum allowable tensile strain without compromising the interleaved structure is defined by $\varepsilon_{max} = L_{overlap}/L$, where $L_{overlap}$ represents the initial overlapping length of two zigzag strips, and L is the initial length of the interleaved assemblies. Placing an interleaved assembly on an elastomeric substrate, anchored at two ends (Fig. 1a), results in a strip exhibiting two distinct tensile rigidity (soft or stiff) on a soft substrate. Extensive research has been conducted on such systems, particularly focusing on the behavior when a pre-stretched substrate (defined by $\varepsilon_{pre} = \Delta L_s/L_s$ where L_s is the initial length of the soft substrate, and ΔL_s is its deformation) releases its strain. This release leads to the buckling of stiff strips adhered to the soft substrate[48,49].

Contrasting with the traditional methods that utilize thin strips with constant tensile rigidity, the present system introduces an additional design variable: jamming-induced tunable tensile rigidity. This variable significantly diversifies the buckling behavior of the system. The buckling height varies depending on the specific moment when the interleaved assembly is jammed, forming a stiff strip on a soft substrate that is releasing strain (Fig. 1d and Supplementary Movie 1). To effectively represent the temporal aspects of jamming and its associated buckling behavior, we introduce the notations $[\varepsilon^R_{pre}]$ and [-]. Notation $[\varepsilon^R_{pre}]$ signifies the state of being jammed at a particular residual pre-strain ε^R_{pre} ($\varepsilon^R_{pre} < \varepsilon_{pre} < \varepsilon_{max}$). This residual pre-strain ε^R_{pre},

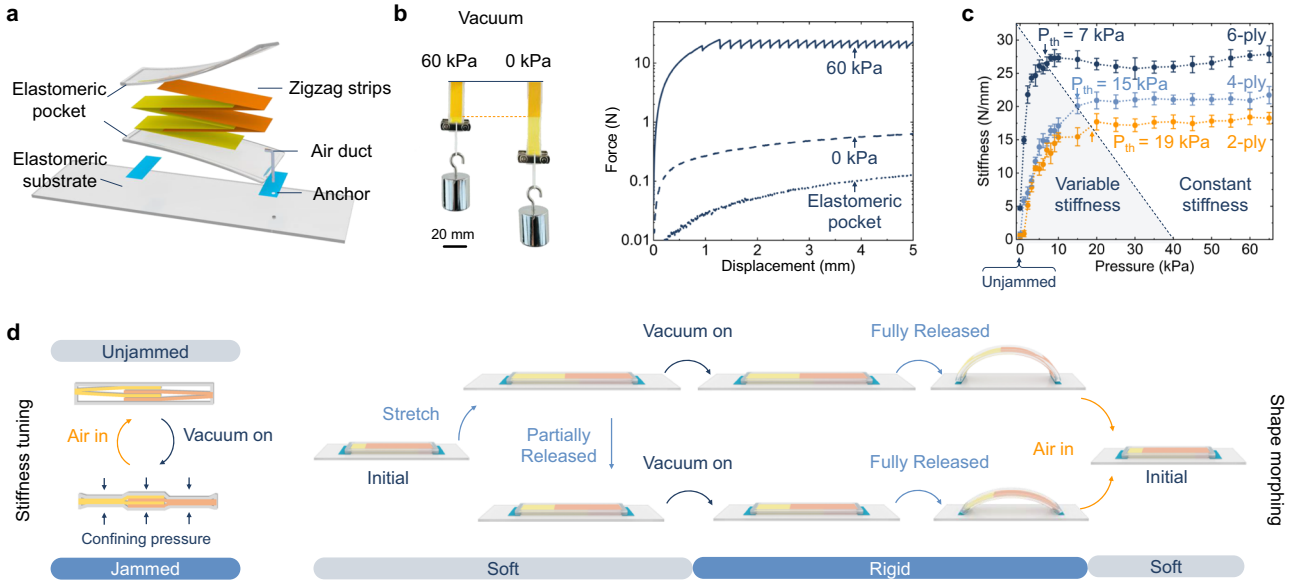

Fig. 1 | Jamming of interleaved papers for stiffness variation and the implementation of a tunable buckling design strategy. a An exploded-view schematic illustration showing an interleaved assembly on an elastomeric substrate, anchored at both ends. **b** Upon application of vacuum, the interleaved zigzag strips yield high stiffness through friction, increasing tensile rigidity of the interleaved assembly. At atmospheric pressure, the interleaved zigzag strips can easily slide over each other. Left, with a mass of 100 g attached to its end, the jammed interleaved assembly almost maintained its initial length, while the unjammed interleaved assembly was easily stretched. Right, the tensile tests show that the jammed interleaved assembly (at vacuum pressure of 60 kPa) is more than 30 time stiffer than the unjammed counterpart. **c** Tensile rigidity versus applied vacuum pressure for interleaved assemblies with varying plies. The data are presented as mean ± s.d. of 3 independent measurements. **d** Schematic illustration of the refreshable buckling behavior enabled by jamming induced tunable tensile rigidity. Left, upon application of vacuum, the stretched state of the interleaved assembly is locked without external loadings. Right, varying the temporal instant to jam the interleaved assembly to form a stiff strip on a strain-releasing soft substrate system, different buckling height are achieved. The continuum energy input is not required to maintain the buckled height and the buckled strip will recover to flat configuration when vacuum is released. Source data are provided as a Source Data file.

in combination with the geometrical parameters of the interleaved assemblies, determines the buckling height h. Conversely, [-] indicates the state of being unjammed, where the '-' symbol is used because ε_{pre}^{R} is no longer relevant in this scenario.

In scenarios where there are arrays of these interleaved assemblies, each individual assembly can be jammed at different temporal instants, enabling a spatiotemporally controllable buckling strategy for fabricating 3D architectures. To represent the spatial and temporal aspects of jamming and buckling, we introduce a matrix **M**, with the subscript "*ij*" indicating the distribution of these arrays on the corresponding 2D plane. In this matrix, each element M_{ij} is denoted by either ε_{pre}^{R} or '-', representing the jammed or unjammed state of each interleaved assembly, respectively. Therefore, matrix **M** functions as an operational guide, dictating that at a specific temporal instance (i.e., ε_{pre}^{R}), a designated assembly (indexed as "*ij*" in **M**) begins to buckle. This approach outlines a design and control strategy for dynamically refreshable 3D structures using spatiotemporally jammed interleaved assemblies. This strategy offers two significant advantages: (1) The jamming process is reversible. When a buckled strip in the ON state is unjammed (by removing the vacuum to revert to the OFF state and allowing air in), it reverts to its original flat configuration. (2) Continuous energy input is not required once the assembly is jammed, making this method energy-efficient for altering the tensile rigidity. It should be noted that the jamming needs to be triggered by a vacuum pump with energy consumption, but once the jamming is complete, the vacuum pump is shut down and the jamming state can be maintained due to the airtight conditions. The sealing tests show that the designed variable-stiffness interleaved assemblies exhibit great airtight performance (see Methods for details).

Figure 2a showcases an example of such a structure with a 3 × 3 array. By applying various operation matrices, we can achieve different configurations (see Methods for details). Supplementary Movie 2 demonstrates the structure's ability to continuously change shape and recover, indicating the potential for creating a vast array of diverse 3D configurations. When the spatial arrangement of these interleaved assemblies is designed to resemble specific shapes, such as animals, the dynamic refreshability imparts a "living" characteristic to the structure. For instance, Fig. 2b illustrates a turtle-shaped structure composed of four angled interleaved assemblies (see Methods for details). Different gestures of this turtle-shaped structure emerge depending on the applied operation matrices. By sequentially applying varied operation matrices, we can simulate a "live turtle" (Supplementary Movie 3). This capability opens up a vast design space for complex and "living" 3D structures, which we discuss in detail in the following section.

When numerous interleaved assemblies are pixelized, the structure can form highly complex shapes using a carefully designed operation matrix **M**. This approach offers a practical solution for large-scale dynamic shape morphing and has the potential for widespread applications. As illustrated in Fig. 2c, these applications could range from education for the visually impaired to remote interaction.

Design and implementation of complex and "live" 3D structures

We modeled each interleaved element at the jammed state as a beam with non-uniform thickness, allowing us to theoretically determine its buckling height (see Methods for details). To further characterize the buckling behavior and capture more intricate details, finite element analysis (FEA) was conducted (see Methods for details). Figure 3a illustrates the relationship between buckling height and residual pre-strain ε_{pre}^{R} for a symmetrically arranged interleaved paper. The specific geometries considered include a 0.5 mm-thick elastomeric pocket and interleaved assemblies measuring 7 mm in width and 19 mm in length,

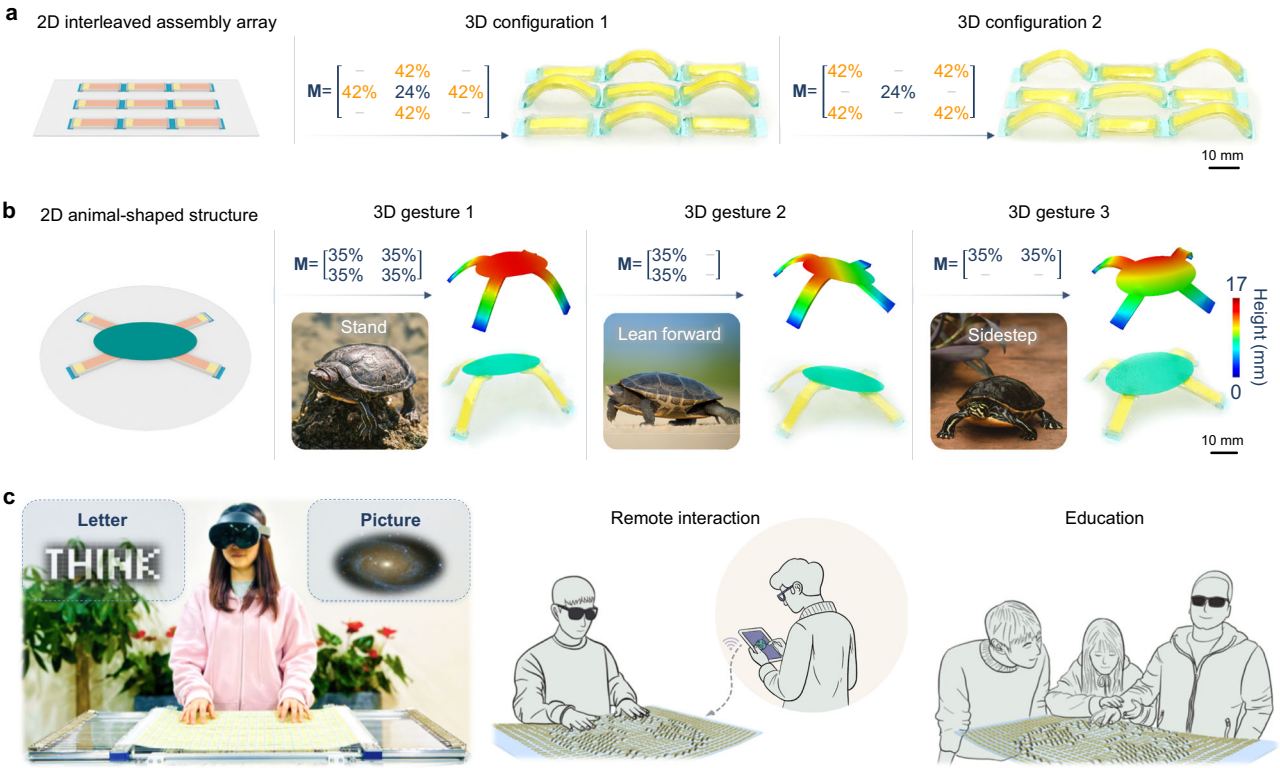

Fig. 2 | Dynamically refreshable 3D structures enabled through a spatiotemporal buckling design strategy. a Schematic of a flat 3 × 3 interleaved assembly array, with experimental results showing two distinct 3D configurations under different operation matrixes **M**. **b** Schematic illustration of a flat animal-shaped structure with four angled interleaved assemblies, with FEA and experimental results showing three different 3D configurations under different operation matrices **M**. The formed 3D configurations mimic the postures of a turtle. **c** Photograph and schematic illustration of a tactile display formed by a 32 × 24 interleaved assembly array for potential applications in remote interaction and visual impaired education.

https://doi.org/10.1038/s41467-024-51865-x

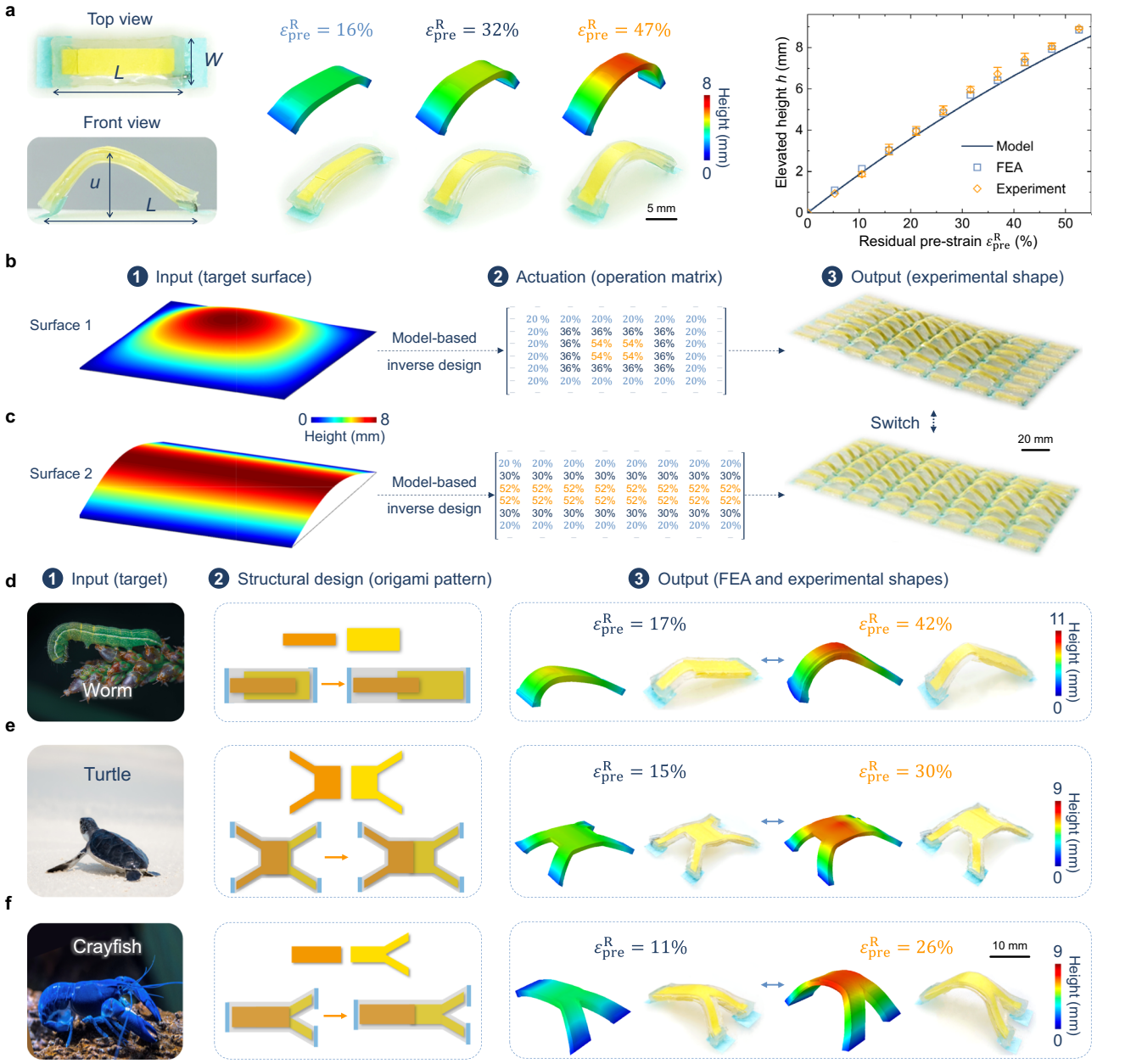

Fig. 3 | Inverse design for complex 3D structures. a Finite element analysis (FEA), experimental, and theoretical results for the maximum buckling height of the interleaved assembly as a function of the residual pre-strain ε^R_{pre}. The data are presented as mean ± s.d. of 3 independent measurements. **b, c** A flow diagram of the model-based inverse design for a pixelized structure consisting of an 8 × 8 array to morph into two distinct target shapes. A flow diagram of the inverse design for the pattern of interleaved assembly to morph into intricate 3D gestures of animals including a worm (**d**), a turtle (**e**), and a crayfish (**f**). Source data are provided as a Source Data file.

with zigzag strips of 5 mm width, 14 mm length, and an initial overlapping length of 11 mm between two strips. It is found that the theoretical model and the finite element simulations agree very well with the experiments (Fig. 3a and Supplementary Fig. 2), which validates the feasibility of inverse design for these structures. Additionally, the mechanical behavior of the buckled interleaved assembly is also tested (Supplementary Fig. 3), revealing a maximum resisting loading of approximately 0.3 N, which is comparable to the force exerted by a typical mouse click or a keyboard typing. And increasing the residual pre-strain (or the buckled height) can enlarge the resisting force. This desirable load-bearing capability of the interleaved assembly suggests a promising potential application in tactile displays.

To achieve a given target shape, such as the one depicted in Fig. 3b with its height represented by contour colors, we first obtain its 3D profile and express it as a numerical table, denoted as $z_{target} = f(x,y)$. Here the dimensions of the table (i.e., $x \times y$) correspond to the size of the pixelized structure. Utilizing the one-to-one relationship between the buckling height and the residual pre-strain ε^R_{pre} as shown in Fig. 3a, we determine the specific residual pre-strain ε^R_{pre} at each spatial location (x, y). The varying ε^R_{pre} values represent the different temporal instants at which each individual interleaved assembly is jammed. Consequently, this process results in the formation of the operation matrix **M**. Guided by the operation matrix **M**, we experimentally realized the 3D shape, achieving $z_{exp} = g(x,y)$. Figure 3b, c illustrates a pixelized structure consisting of an 8 × 8 array morphing into two different target shapes, based on this inverse design strategy. The operation matrices and detailed morphing processes for these shapes are presented in Supplementary Fig. 4 (also see Supplementary

Movie 4). To evaluate the accuracy of the inverse design, we employ an error function $e = |z_{target} - z_{exp}|/z_{target}$ as detailed in Supplementary Fig. 4. Here, the primary source of errors is the manually fabricated interleaved assemblies, which can lead to inconsistencies with the theoretical assumptions.

Beyond achieving 3D configurations with symmetric interleaved papers (as shown in Fig. 3a) and their array-like designs (e.g., Fig. 2a, b), our approach enables the construction of more intricate 3D shapes. This is achieved by incorporating various 2D interleaved assemblies, which can be designed through an intuitive inverse design process. Figure 3d–f showcases some exemplary creations, including a worm (Fig. 3d), a turtle (Fig. 3e), and a crayfish (Fig. 3f). For each of these examples, we provide the target shapes, the corresponding simulations, and the experimental results. Besides, the helix-shaped and mouth-shaped 3D architectures with complex twisting deformation can also be obtained (Supplementary Fig. 5). These comparisons demonstrate a high fidelity in 3D shape reproduction, underscoring the effectiveness of our design and fabrication approach.

Control of pixelized interleaved assembles for large-scale and dynamic 3D reconstruction

With the help of the inverse design, we can construct large scale and intricate 3D shapes by spatiotemporally buckling multiple interleaved assemblies (e.g., over 500) placed on soft substrates. This approach even allows for the transformation of 2D images into 3D structures. A key challenge in this process is efficiently controlling and accessing each individual interleaved assembly. Figure 4a shows a pneumatic control unit designed for an 8 × 8 array of interleaved assemblies, enabling individual control of these 64 units using just a single solenoid valve (see Methods and Supplementary Fig. 6 for details). In this

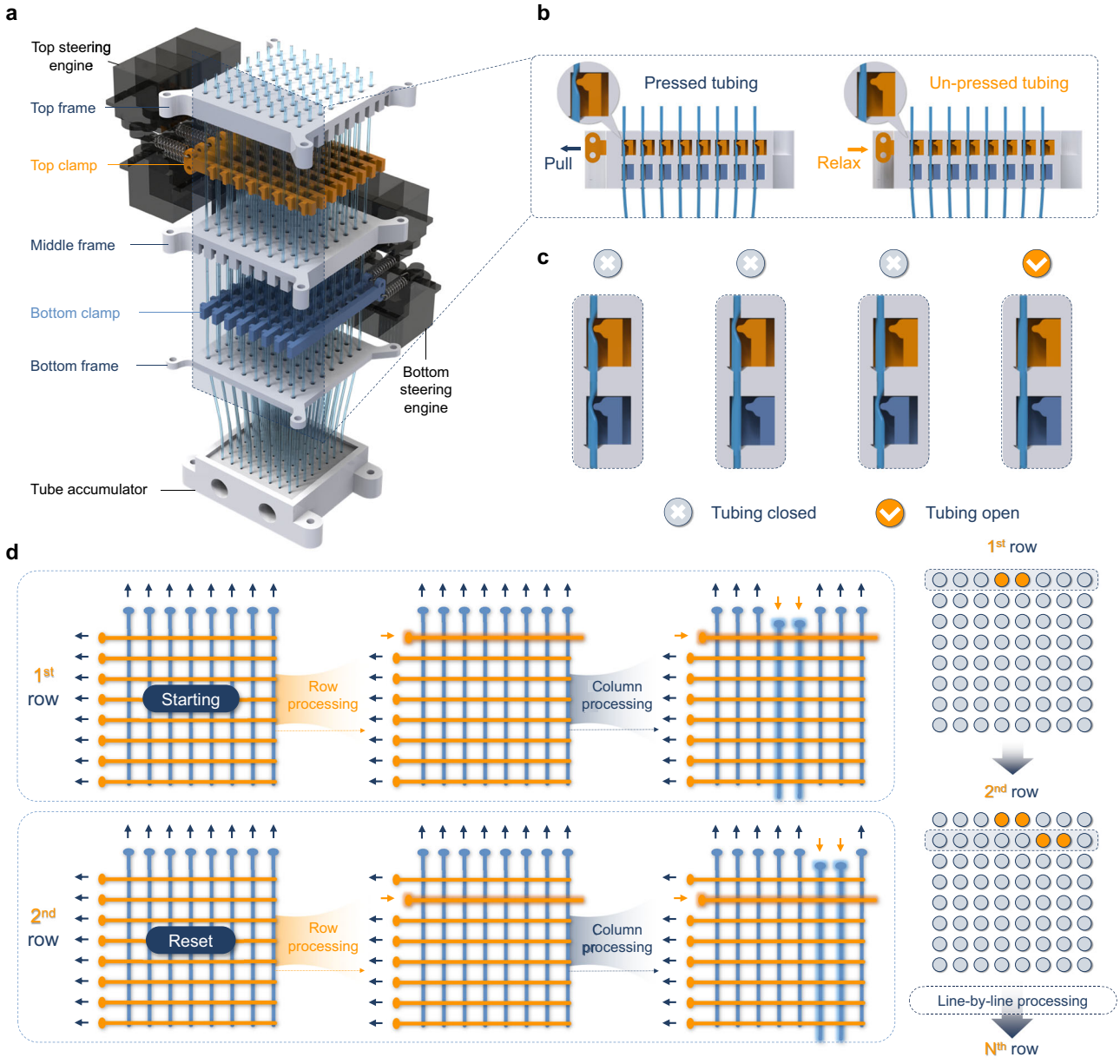

Fig. 4 | Operating principle of pneumatic control. a An exploded-view schematic illustration of a pneumatic control unit for an 8 × 8 interleaved assembly array. **b** A cross-sectional schematic illustration of the pneumatic control unit in the pulling and relaxing states. **c** A schematic illustration showing the tube in open or close states controlled by perpendicular top and bottom clamps. **d** A schematic outlining the process of line scanning mechanism to individually control the 8 × 8 interleaved assemblies using 2 × 8 steering engines, illustrating the system's efficiency in managing a large number of units.

https://doi.org/10.1038/s41467-024-51865-x

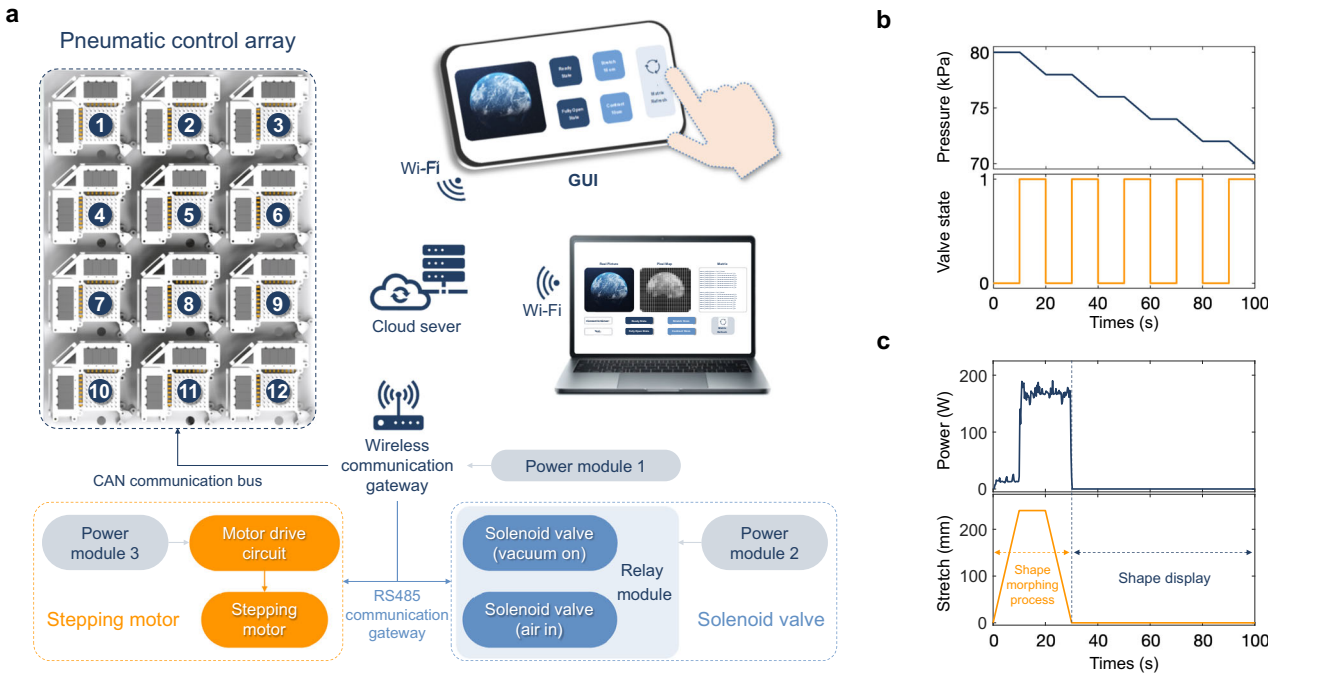

Fig. 5 | Control strategies for a large-scale, pixelized array of interleaved assemblies. a A circuit diagram and connection mechanisms of a 32 × 24 interleaved assembly array and its wireless interface to a touchscreen device or a laptop. **b** Pressure response of the pneumatic control unit (top panel) under given control command (bottom panel). The pneumatic control unit has two states, i.e., '0' state (or OFF state) for tubing closed and '1' state (or ON state) for tubing open, which leads to constant or decreased pressures, respectively. The switch of the state of the pneumatic control unit can precisely and quickly vary the pressure response. **c** Power consumption of the actuation system. During shape-morphing process (e.g., the display of a word "THINK"), the operation of the stepping motor and the steering engines causes transient energy consumption. While during prolonged shape-display process, there is no energy consumption.

system, the 64 tubes are collectively controlled as a group through a bottom tube accumulator, which is set to ON or OFF by the solenoid value, and the individual access to each assembly is achieved through eight bottom clamps and eight top clamps arranged perpendicularly. These clamps can be pulled or relaxed by steering engines. As depicted in Fig. 4b, a tube is closed upon pulling and opened upon relaxing. Therefore, when both top and bottom clamps for a specific tube are relaxed, it opens, as shown in Fig. 4c. This arrangement of perpendicular top and bottom clamps introduces an efficient line scanning mechanism for individual control of each interleaved assembly, as illustrated Fig. 4d. To operate the 1st row, for instance, all clamps are initially pulled to close all tubes. The process then involves relaxing the clamps of the 1st row (row processing) followed by relaxing the clamps of the required columns (column processing), such as the 4th and 5th columns in this example. The completed operation for the 1st row results in the vacuuming and jamming of the interleaved assemblies at the (1st row, 4th column) and (1st row, 5th column) positions. After completing a row, all clamps are reset to the pulled position, and the process is repeated for subsequent rows until the entire array is addressed. It should be noted that a pneumatic control system consisting of 32 rows and 24 columns can be designed to simplify the present pneumatic actuation system, which directly controls 32 × 24 interleaved assemblies without modular design of pneumatic control units. To this end, more powerful and efficient steering engines are imperative to ensure that the tubes can be closed effectively.

Figure 5a illustrates the overall control diagram, showcasing three primary control modules: the solenoid valve module, the stepping motor module, and the pneumatic control array module. The central communication module processes the image information and orchestrates the operations of the solenoid valve module, stepping motor module, and pneumatic control array module (see Methods and Supplementary Fig. 6 for details). Here, the pneumatic control array module is capable of managing an array of 32 × 24 interleaved assemblies, which are organized into 4 × 3 pneumatic control units. The performance of the pneumatic control unit has been tested. As demonstrated in Fig. 5b, the open/closed states of the tube can be regulated rapidly and with high precision (see Methods and Supplementary Fig. 7 for testing details). It is important to note that the jamming mechanism allows the formed 3D shapes to be maintained without the need for continuous energy input. Specifically, after the elastomeric substrate is fully released and the 3D shapes are constructed, the pneumatic control is shut down to cause jamming for all interleaved assemblies, which cannot vary the formed 3D shapes. Thus, the stepping motor and the steering engines of the pneumatic control array are activated only when there is a need to alter the 3D shape. As shown in Fig. 5c, power consumption occurs solely during the refreshing of the 3D shape, which results in an energy-efficient system for shape display.

Refreshable, intricate shape morphing of large-scale, pixelized interleaved assemblies

Figure 6a presents a schematic illustration of the present highly integrated shape-morphing system, showcasing the dynamic 3D metasurface and its associated control modules, designed to exhibit a wide range of intricate shape transformations. A large-scale array consisting of 768 interleaved assemblies, as depicted in Fig. 6b (see Methods and Supplementary Fig. 8 for fabrication details), was fabricated. Utilizing the inverse control process, we transformed color images into 3D metasurfaces using the designed large-scale, pixelized interleaved assemblies (see Methods and Supplementary Fig. 9 for details). Figure 6c–e showcases the photographs of the 32 × 24 array morphing into various shapes, including a word "THINK", a representation of planet earth, and a galaxy, juxtaposed against their targeted images, with Supplementary Movie 5 presenting the dynamic refreshing processes. For the word of THINK and the representation of planet earth, a uniform height of 8.1 mm was set for the buckled interleaved

https://doi.org/10.1038/s41467-024-51865-x

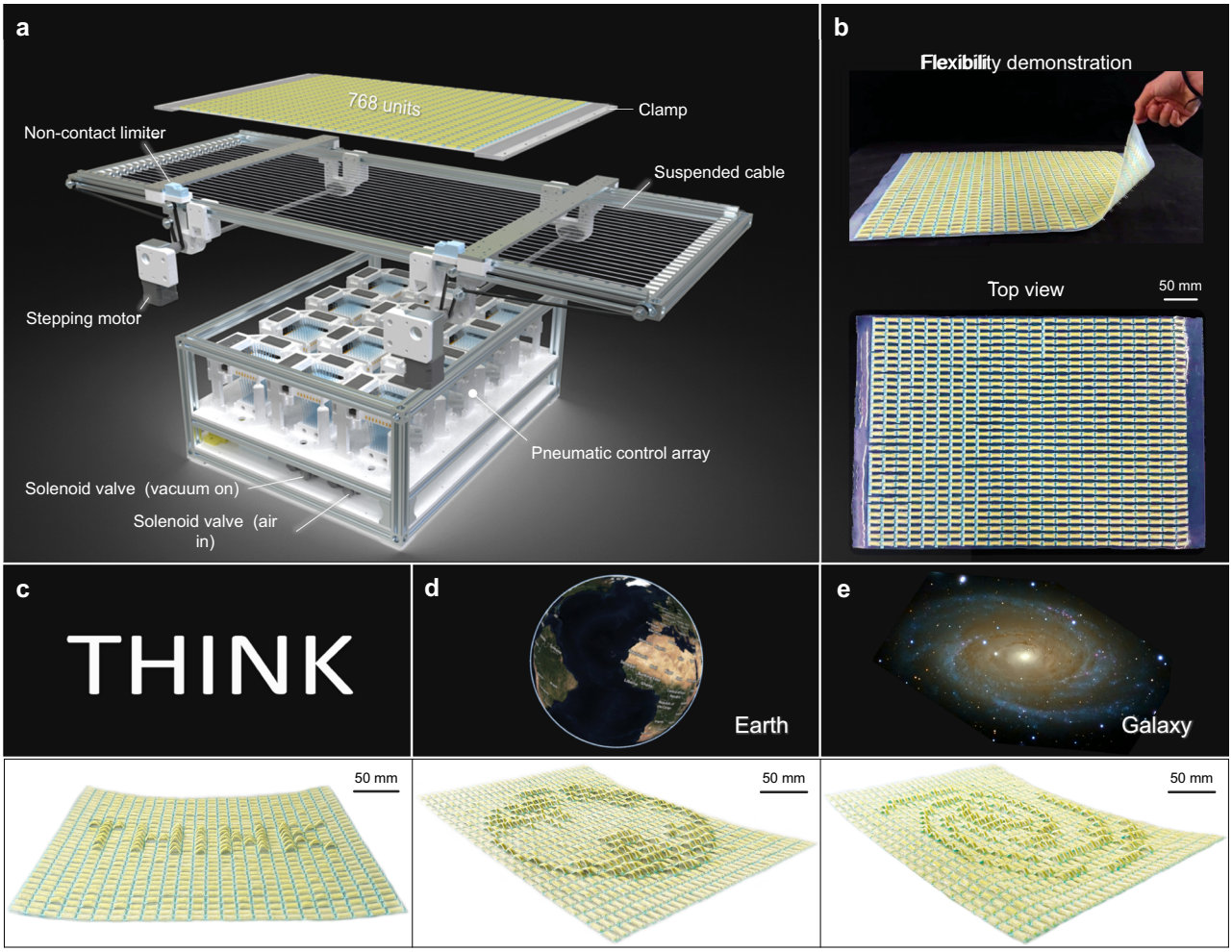

Fig. 6 | Refreshable and intricate shape morphing of large-scale, pixelized interleaved assemblies. a An exploded-view schematic illustration of the shape-morphing system. **b** Photograph showing a 32 × 24 interleaved assembly array in the peeling state (top panel) and flat state (bottom panel). Experimental results of a 32 × 24 interleaved assembly array morphing into (**c**) a word "THINK", (**d**) a representation of planet earth, and (**e**) a shape of galaxy.

assemblies. For the shape of galaxy, two different heights of 8.1 mm and 5.6 mm were used, with the larger height in the central region of the 3D metasurface to correspond to the brighter part of the color image.

User study: tactile shape recognition via dynamic 3D metasurfaces

We conducted a user study involving 14 visually impaired subjects to evaluate the effectiveness of our device in assisting with graphical information recognition, a crucial skill for enhancing independence and the quality of life for individuals with visual impairments. The study comprised two perception experiments to evaluate recognition accuracy and time efficiency, followed by a questionnaire designed to gauge subjective experiences (see Methods for details).

Figure 7a depicts a participant using our wirelessly controlled 3D metasurface device to recognize five geometric shapes. In Fig. 7b, c, confusion matrices compare the true versus perceived shapes, revealing an increase in mean recognition accuracy when the buckling height increased from 5.6 mm to 8.1 mm, particularly for the ellipse shape. This demonstrates the participants' ability to distinguish between different shapes and highlights the importance of buckling height in shape recognition. Figure 7d, with further details in Supplementary Figs. 10 and 11, and Tab. 1, shows significant improvements in shape recognition efficiency with increased buckling heights, underscoring the device's effectiveness in enhancing spatial perception for visually impaired users. Figure 7e illustrates the NASA-TLX results across six dimensions, where a low overall mean score indicates a moderate workload (see more details in Supplementary Fig. 10). The highest mean scores were observed in own performance (D4) and mental demand (D2), suggesting a high level of cognitive engagement, while physical (D1) and temporal demands (D3) were comparatively lower, with minimal frustration (D6) reported. Overall, the user study validates that the dynamic 3D metasurfaces can substantially aid visually impaired individuals in recognizing graphical information, paving the way for innovative accessibility applications for the visually impaired community.

Discussion

This work introduces a straightforward strategy for achieving load-bearing, dynamically refreshable, intricate shape morphing from initially flat soft structures. The pivotal feature of this approach lies in the selective stiffening of the interleaved assemblies through jamming at different spatial locations and in different temporal instants during the relaxation of a pre-stretched soft substrate. This process results in a diverse range of 3D architectures from a single array of interleaved assemblies. A notable advantage of our method is the reversible and rapid nature of the jamming-based tunable stiffness, which importantly does not require energy to maintain its form once set, thus facilitating sustained shape display in an energy-efficient manner and allowing for easy reversion to the original flat state. Additionally, unlike

https://doi.org/10.1038/s41467-024-51865-x

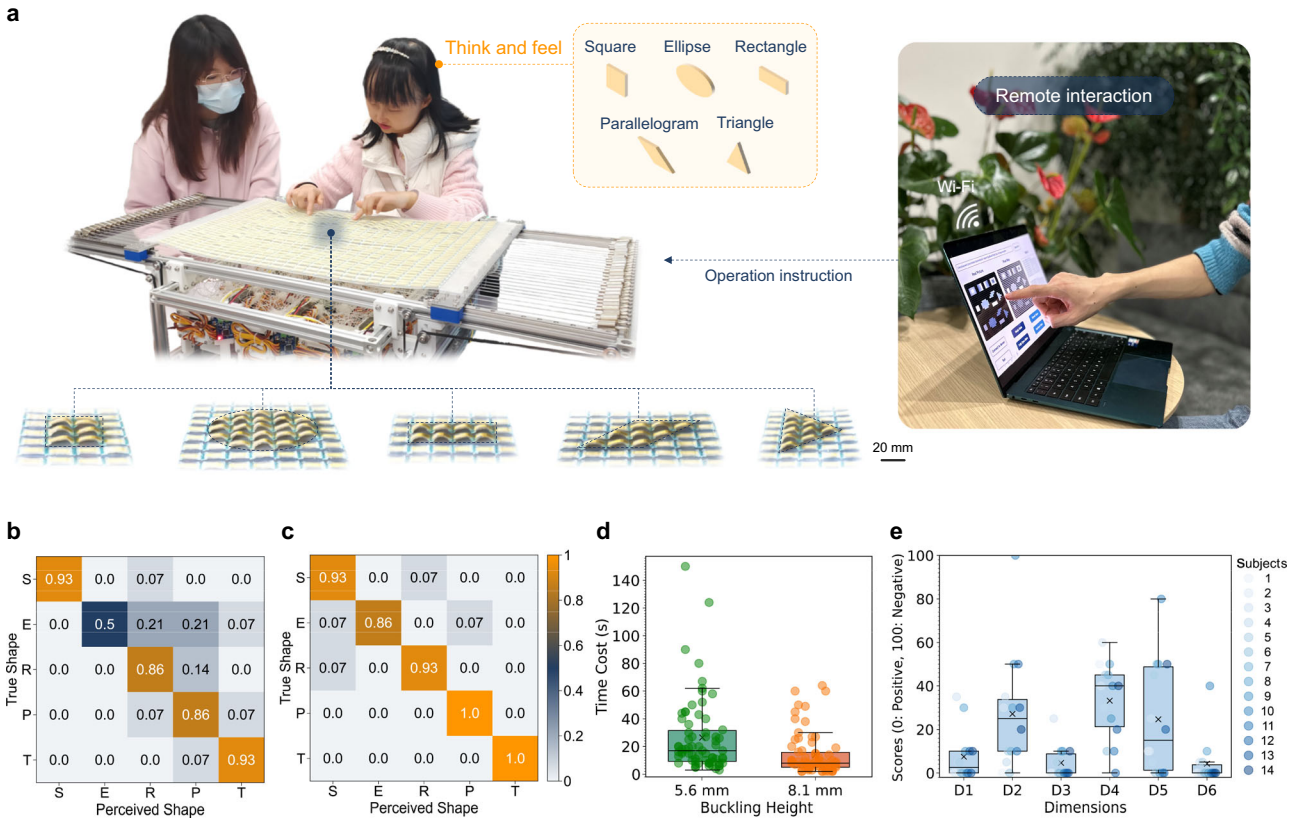

Fig. 7 | User study on the dynamic 3D metasurface device for assisting visually impaired individuals. a A photograph shows a visually impaired participant engaged in shape recognition tasks using the wireless controlled 3D metasurface device. **b**, **c** Confusion matrices of recognition accuracy from Experiments 1 and 2, respectively. The buckling height increased from 5.6 mm in **b** to 8.1 mm in **c**. The letters represent different shapes: "S" for square, "E" for ellipse, "R" for rectangle, "P" for parallelogram, and "T" for triangle. These results highlight the impact of buckling height on recognition accuracy. **d** Statistical results of time cost indicating highly significant improvements in recognition efficiency with increased unit heights ($n = 14$, 8 males, 6 females, ages 26–56; $p < 0.001$, Paired-samples Wilcoxon Test; whiskers, 5–95 percentile; boxes, interquartile; horizontal lines, medians; cross mark, means; circular scatter, time cost for perceiving each shape by each subject). **e** Statistical results of NASA-TLX questionnaires indicating a moderate workload of the 3D metasurface device. (D1: physical demand, D2: mental demand, D3: temporal demand, D4: performance, D5: effort, D6: frustration). Source data are provided as a Source Data file.

shape-morphing strategies that use multi-stable structures, which are limited to transitions between multiple discrete states, our method offers the capability to alter configurations in a continuous manner. This feature allows for more versatile and diverse shape morphing compared to the constrained nature of multi-stable structures.

Our theoretical model accurately predicts the buckling height of jammed interleaved assembly, which provides a quantitative foundation for inverse design to precisely achieve desired 3D architectures. Several interesting bioinspired 3D architectures are also constructed by inverse design of the origami patterns, which is difficult to be achieved using the traditional simple airbag structures. We have successfully implemented the inverse-design model in a tightly integrated shape-morphing metasurface system, comprising an array of 768 interleaved assemblies and corresponding control modules, to construct large-scale and intricate 3D shapes. Furthermore, the practical application of our dynamic 3D metasurface as a tactile display for the visually impaired is preliminarily demonstrated through five typical geometrical shapes with 2D features. We expect that the future work will include user study involving complex 3D shapes to further validate that the proposed dynamic 3D metasurfaces can aid visually impaired individuals in learning.

The current jamming-based stiffness tuning method limits the miniaturization and precise customization of dynamic 3D metasurfaces, as the manual fabrication technique imposes a minimum assembly size of approximately 15 mm and inevitable manufacturing error. This is indeed an intractable issue and weakens the performance of continuous height control. To overcome this limitation, we propose the use of alternative variable-stiffness technologies, such as shape memory polymers[50] or low melting point alloys[30]. These materials could facilitate the development of miniaturized and customized buckling structures, thereby broadening the potential for enhancements and increasing the diversity of applications. The principles and methodologies presented here outlines a promising route towards the fabrication of large-scale, dynamically refreshable 3D metasurfaces, capable of replicating complex shapes for a wide range of applications across various fields.

Methods

Our user study has received approval from the Westlake University's Ethical Review Board (approval number: 20230731JHQ001), and all participants provided informed consent.

Fabrication of interleaved assemblies and shape-morphing structures

Interleaved assemblies. The fabrication process for the variable-stiffness interleaved assemblies began with the preparation of airtight elastomeric pockets. These molds were 3D printed using polylactic acid (PLA+, eSun) using an FDM 3D printer (Pro3plus, Raise3D). Soft silicone elastomer (Ecoflex 00-30, Smooth-On) was then cast into the 3D-printed molds to create elastomeric pockets with a thickness of 0.5 mm. Subsequently, 0.075-mm-thick sheets of copy paper (M&G

Multipurpose Colored Copy Paper) were cut into strips using a Cameo 3 cutter (Silhouette American). These strips were manually folded to form zigzag patterns, which can vary in design as shown in Fig. 3d–f. Note that, other flexible materials such as polyvinyl chloride (PVC), polypropylene (PP) and polyethylene (PE) can also be used to design the folded zigzag strips. Silicone adhesive (Sil-poxy, Smooth-On) was applied to the sides and ends of the elastomeric pocket, and the folded zigzag strips, along with a tubular air duct, were positioned onto it. To complete the assembly, another elastomeric pocket was placed on top, and slight compression was applied to ensure airtight sealing.

Shape-morphing structures. The stretchable substrates were cast from soft silicone elastomer (Dragon Skin 20, Smooth-On) using 3D-printed molds. The interleaved assemblies were securely attached to the stretchable substrates through two anchor points made of copy paper. These points, located at the ends of the assemblies, were affixed using silicone adhesive, ensuring firm attachment, and facilitating effective shape morphing.

Mechanical characterization and sealing test of interleaved assemblies

Tensile tests. The force-displacement relationships of the variable-stiffness interleaved assemblies were determined using uniaxial tension tests (Instron 6800, Illinois Tool Works), with displacement controlled at a loading rate of 5 mm min^{-1}. The interleaved assemblies were connected to a vacuum pump (750D, Fujiwara), and a manual vacuum regulator (IR1000-01-A, SMC) was employed to set the desired vacuum pressure (Supplementary Fig. 1a). Specifically, three separate tensile tests were repeated at each vacuum pressure.

Calculating the interleaved assemblies' tensile stiffness. To calculate the tensile stiffness of the interleaved assemblies (Fig. 1c), we performed linear fitting of the force–displacement curves (Supplementary Fig. 1) at small tension displacements. The slope of the linear fitting curves was calculated as the tensile stiffness. And the tensile stiffness shown in Fig. 1c were the average values from three separate experiments.

Samples for characterizations of tensile stiffness. We fabricated three groups of interleaved assemblies with varying layers of zigzag strips (e.g., 2 plies, 4 plies and 6 plies). The dimensions of the zigzag strips were 40 mm in length and 10 mm in width, with an initial overlapping length of 20 mm between two strips. The tensile stiffness of these interleaved assemblies was measured under different vacuum pressures.

Sealing test. Initially, the flat interleaved assembly was actuated to assume an elevated configuration. Following this, the vacuum pump was turned off to stop the vacuum input. The airtight performance was then evaluated by monitoring the height variation of the interleaved assembly over time. In our tests, the height of the interleaved assembly did not show significant changes after 24 hours.

3 × 3 array fabrication and actuation

Fabrication. The geometry of the overlapped strips is designed with dimensions of 5 mm in width and 14 mm in length, featuring an initial overlapping length of 11 mm. The resulting interleaved assembly measures 7 mm in width and 19 mm in length. The silicone elastomer substrate is 1 mm thick, 150 mm long, and 40 mm wide. Additionally, the paper anchors employed have dimensions of 7 mm in length and 5 mm in width. In the configuration of these nine interleaved assemblies, the horizontal and vertical gaps between adjacent assemblies are maintained at 3 mm and 5 mm, respectively.

Actuation. The shape morphing of the 3 × 3 array was initiated by stretching the substrate to a prescribed pre-strain using a uniaxial stage (SGX-1605, Yongjia). After stretching, the substrate was released, and based on the predetermined operation matrices, interleaved assemblies at various locations were jammed by applying vacuum at different levels of residual pre-strain. Each interleaved assembly was connected to a solenoid valve (VK332V-5G-01, SMC) to preciously control the vacuum input, with the vacuum being supplied by a vacuum pump. To revert the structure to its initial flat configuration, the substrate was slightly stretched again, and the vacuum was neutralized by introducing air back into the interleaved assemblies.

Animal-shaped structure fabrication and actuation

Fabrication. The geometry of the overlapped strips is designed with a width of 5 mm and a length of 18 mm, featuring an initial overlapping length of 12 mm. The dimensions of the interleaved assembly are 7 mm in width and 24 mm in length. The substrate, made of circular silicone elastomer, measures 1 mm in thickness and 140 mm in diameter. Paper anchors used in the assembly are 7 mm long and 5 mm wide. Additionally, an elliptic panel made of polyvinyl chloride (PVC) with a thickness of 0.5 mm, a length of 40 mm, and a width of 20 mm was prepared. This panel was adhered to the opposite end of four interleaved assemblies using silicone adhesives.

Actuation. The transformation of a flat structure into various 3D animal-shaped architectures begins with stretching the silicone elastomer substrate to a predetermined pre-strain, achieved using a customized biaxial stage. Through this biaxial stretch, we manage the elongation and release of four angled interleaved assemblies along their axial directions. Control over the axial strain of the interleaved assemblies allows for the formation of 2D animal-shaped structures (Fig. 2b), similar to the 2D interleaved assembly array shown in Fig. 2a, using the defined operation matrix **M**. Specifically, during the stretching process, the four interleaved assemblies are sequentially jammed in a specific order as dictated by the designated operation matrices. Releasing the pre-strain subsequently triggers the transformation into the 3D architecture. To revert the structure to its initial flat configuration, the substrate is stretched again, the vacuum is removed, and finally, the substrate is fully released.

Analytical model

We consider the jammed interleaved assemblies as a three-segment beam with non-uniform thickness. As depicted in Supplementary Fig. 2a, the initial lengths of segments 1 and 2 are denoted as L_1 and $2L_2$, respectively. After stretching and jamming the assemblies at a pre-strain ε_{pre}^{R}, the lengths of these segments change to l_1 and $2l_2$. Consequently, the pre-strain is defined as $\varepsilon_{pre}^{R} = (l - L)/L$, where $L = 2L_2 + L_1$ and $l = 2l_2 + l_1$.

Upon releasing the pre-stretched substrate, the straight jammed interleaved assemblies transform into a curved configuration through out-of-plane bending. We model this transformation by treating the jammed interleaved assemblies as a simply supported non-uniform beam subjected to a uniaxial compressive force P (Supplementary Fig. 2b). In the following, we use elastica theory and derive the governing equations for the non-uniform beam, which enables us to predict the post-buckling configuration of the jammed interleaved assemblies.

As illustrated in Supplementary Fig. 2b, we establish a Cartesian coordinate system to analyze the beam's behavior. In this system, s represents the arc distance measured along the axis of the beam from the origin o. The variable φ denotes the tangential angle formed between the neutral axis of the beam and the x-axis. The geometrical relationships between the displacement components of the beam and

the tangential angle φ are determined by the following equations:

$$\frac{\mathrm{d}x}{\mathrm{d}s} = \cos\varphi, \tag{1}$$

$$\frac{\mathrm{d}y}{\mathrm{d}s} = \sin\varphi. \tag{2}$$

The differential equation of the deflection curve is

$$(EI)_j \frac{\mathrm{d}\varphi}{\mathrm{d}s} = -Py, \tag{3}$$

where $(EI)_j$ is the equivalent bending stiffness of the segment j. Here, for the sandwich beam (i.e., silicone/paper/silicone) used in our design, the equivalent bending stiffness can be expressed as

$$(EI)_1 = \frac{1}{12}E_p w\left(nt_p\right)^3 + \frac{1}{6}E_s w t_s^3 + 2E_s w t_s\left(\frac{t_s + nt_p}{2}\right)^2, \tag{4}$$

$$(EI)_2 = \frac{1}{12}E_p w\left(2nt_p\right)^3 + \frac{1}{6}E_s w t_s^3 + 2E_s w t_s\left(\frac{t_s + 2nt_p}{2}\right)^2, \tag{5}$$

where n is the number of layers of a zigzag strip, E is the Young's modulus, t is the thickness, w is the width of the beam, with subscripts p and s for the paper and the silicone elastomer, respectively.

Using Eqs. (3)–(5), the following equation is derived

$$\frac{\mathrm{d}\varphi}{\mathrm{d}s} = \begin{cases} \frac{-Py}{(EI)_1}, 0 \le s \le l_1, \\ \frac{-Py}{(EI)_2}, l_1 \le s \le l_1 + l_2. \end{cases} \tag{6}$$

Equations (1), (2) and (6) can be employed to derive the deformed deflection curve of the non-uniform beam. Besides, the boundary conditions are

$$x(s=0) = 0, y(s=0) = 0, \varphi(s=0) = \varphi_0, \varphi\left(s = l/2\right) = 0, \tag{7}$$

where φ_0 is the tangential angle of the beam at the origin o. In addition, the endpoint of the segment 1 and the origin of the segment 2 should yield the continuity of the deflection and slope.

For segment 1 ($0 \le s \le l_1$), by eliminating s between Eqs. (2) and (6), y is obtained as

$$y(\varphi) = \sqrt{y_0^2 + \frac{2(EI)_1}{P}\left(\cos\varphi - \cos\varphi_0\right)}, \tag{8}$$

where y_0 is an integration constant. Then, using Eqs. (1), (6) and (8), x is obtained as

$$x(\varphi) = -\int_{\varphi_0}^{\varphi} \frac{\cos\xi \mathrm{d}\xi}{\sqrt{\left[\frac{P}{(EI)_1}\right]^2 y_0^2 + \frac{2P}{(EI)_1}\left(\cos\xi - \cos\varphi_0\right)}} + x_0, \tag{9}$$

where x_0 is a integration constant. Substituting Eq. (8) into Eq. (6) and integrating, we can obtain

$$s(\varphi) = -\int_{\varphi_0}^{\varphi} \frac{\mathrm{d}\xi}{\sqrt{\left[\frac{P}{(EI)_1}\right]^2 y_0^2 + \frac{2P}{(EI)_1}\left(\cos\xi - \cos\varphi_0\right)}} + s_0, \tag{10}$$

where s_0 is a integration constant. Based on the boundary conditions, the values of x_0, y_0 and s_0 are zero.

Following the procedure presented for the segment 1, the deformed deflection curve of the segment 2 ($l_1 \le s \le l_1 + l_2$) can be determined by

$$y(\varphi) = \sqrt{y_c^2 + \frac{2(EI)_2}{P}\left(\cos\varphi - \cos\varphi_c\right)}, \tag{11}$$

$$x(\varphi) = -\int_{\varphi_c}^{\varphi} \frac{\cos\xi \mathrm{d}\xi}{\sqrt{\left[\frac{P}{(EI)_2}\right]^2 y_c^2 + \frac{2P}{(EI)_2}\left(\cos\xi - \cos\varphi_c\right)}} + x_c, \tag{12}$$

$$s(\varphi) = -\int_{\varphi_c}^{\varphi} \frac{\mathrm{d}\xi}{\sqrt{\left[\frac{P}{(EI)_2}\right]^2 y_c^2 + \frac{2P}{(EI)_2}\left(\cos\xi - \cos\varphi_c\right)}} + l_1, \tag{13}$$

where y_c, x_c and φ_c are the coordinates and the tangential angle of the beam at the endpoint of the segment 1, respectively. In addition, using Eqs. (8) and (9), we have

$$y_c = \sqrt{\frac{2(EI)_1}{P}\left(\cos\varphi_c - \cos\varphi_0\right)}, \tag{14}$$

$$x_c = \int_{\varphi_c}^{\varphi_0} \frac{\cos\xi \mathrm{d}\xi}{\sqrt{\frac{2P}{(EI)_1}\left(\cos\xi - \cos\varphi_0\right)}}. \tag{15}$$

At the midpoint of the beam, the tangential angle φ is equal to 0, and the corresponding vertical displacement is maximal. Using Eqs. (11) and (14), the maximal vertical displacement is

$$y(\varphi = 0) = \sqrt{\frac{2(EI)_1}{P}\left(\cos\varphi_c - \cos\varphi_0\right) + \frac{2(EI)_2}{P}\left(1 - \cos\varphi_c\right)}. \tag{16}$$

Equation (16) contains three unknown parameters φ_0, φ_c and P. To determine these parameters, we apply three constraints. The first two constraints are based on the lengths of the segments. By employing Eqs. (10) and (13), we impose the following constraints

$$l_1 = \int_{\varphi_c}^{\varphi_0} \frac{\mathrm{d}\xi}{\sqrt{\frac{2P}{(EI)_1}\left(\cos\xi - \cos\varphi_0\right)}}, \tag{17}$$

$$l_2 = \int_0^{\varphi_c} \frac{\mathrm{d}\xi}{\sqrt{\left[\frac{P}{(EI)_2}\right]^2\left[\frac{2(EI)_1}{P}\left(\cos\varphi_c - \cos\varphi_0\right)\right] + \frac{2P}{(EI)_2}\left(\cos\xi - \cos\varphi_c\right)}}. \tag{18}$$

The third constraint is that the finial span of the buckled curvy beam should be equal to L, which gives

$$x(\varphi = 0) = \int_0^{\varphi_c} \frac{\cos\xi\,\mathrm{d}\xi}{\sqrt{\left[\frac{P}{(EI)_2}\right]^2\left[\frac{2(EI)_1}{P}\left(\cos\varphi_c - \cos\varphi_0\right)\right] + \frac{2P}{(EI)_2}\left(\cos\xi - \cos\varphi_c\right)}} + \int_{\varphi_c}^{\varphi_0} \frac{\cos\xi \mathrm{d}\xi}{\sqrt{\frac{2P}{(EI)_1}\left(\cos\xi - \cos\varphi_0\right)}} = \frac{L}{2}. \tag{19}$$

By using Eqs. (17)–(19), we can calculate the values of φ_0, φ_c and P at $\varphi = 0$. Subsequently, substituting these three parameters back into Eq. (16) enables us to determine the maximal vertical displacement ($y(\varphi = 0)$) for given values of L_1, L_2 and $\varepsilon_{\mathrm{pre}}^{\mathrm{R}}$. Furthermore, the deflection

of any arbitrary point along the non-uniform beam can be calculated in a similar manner, providing a comprehensive understanding of the beam's deformation under the specified conditions.

Finite element analysis

To accurately capture the mechanical deformations and the resultant 3D structures of the interleaved assemblies, we employed the commercial finite element analysis software ABAQUS. This analysis was conducted during the processes of stretching, jamming, and compressive buckling of the assemblies. Pressure was uniformly applied to all outer surfaces, and the interfaces between the layers were designated as contact surfaces, utilizing a penalty friction formulation for interaction. A uniform mesh was used consisting of eight-node 3D solid elements (C3D8R) with reduced integration. To ensure accuracy, refined meshes were used in areas of interest. Linear elastic constitutive model was used to model the interleaved papers and the PVC panel. The Young's modulus (E) and Poisson's ratio (υ) for the materials were set as follows: $E_{\mathrm{paper}} = 1.01$ GPa and $\upsilon_{\mathrm{paper}} = 0.156$ for copy paper; $E_{\mathrm{pvc}} = 3.14$ GPa and $\upsilon_{\mathrm{pvc}} = 0.4$ for PVC. For the Eco-flex 0030 elastomer, the Ogden hyper-elastic constitutive model was adopted, with material parameters $\mu_1 = 3.46 \times 10^{-3}$ MPa, $\mu_2 = 3.9 \times 10^{-2}$ MPa, $a_1 = 4.18$ and $a_2 = -1.63$.

Valve fabrication and testing

Fabrication. The basic pneumatic control unit capable of controlling the 8 × 8 array of interleaved assemblies (Fig. 4a) was fabricated using a modular strategy. *(1) 3D printing of components:* The top and middle frames (each 68 mm in length and width, and 7 mm in thickness, with holes of 10 mm diameter), bottom frames (68 mm in length and width, and 3 mm in thickness, with holes of 10 mm diameter), clamps (60 mm in length, 10 mm in width, 5 mm in thickness), and tube accumulators (70 mm in length, 50 mm in width, 18 mm in thickness) were 3D printed with photosensitive resin (Somos Imagine 8000, DSM Desotech) through an SLA (stereolithography) 3D printer (Lite 800, UnionTech). *(2) Assembly:* The assembly process included stacking a top frame, a middle frame, and a bottom frame, and then attaching eight top clamps and eight bottom clamps to this stack. *(3) Steering engines installation:* Sixteen steering engines (each 21.5 mm in length, 11.8 mm in width, 22.7 mm in thickness, weighting 9 g, model SG90, Tiankongrc) were inserted into 3D-printed supporting frames. These engines were connected to the clamps using springs. *(4) Tube installation:* Rubber tubes (0.3 mm in inner diameter and 0.8 mm in outer diameter) were threaded through the holes of top, middle and bottom frames. *(5) Final connections:* The rubber tubes were then connected to the tube accumulator, completing the fabrication of a pneumatic control unit (Supplementary Fig. 6).

To control a large-scale interleaved assembly array, the integration of multiple pneumatic control units is necessary. Supplementary Fig. 6 shows an integrated pneumatic control array device, measuring 560 mm in length, 430 mm in width, and 230 mm in height. This device is capable of controlling a 32 × 24 array of interleaved assemblies and is composed of 4 × 3 pneumatic control units. The fabrication process involved the following steps: (1) 12 pneumatic control units were securely fixed onto an acrylic plate. The adjacent tube accumulators were then interconnected using rubber tubes. (2) The acrylic plate with the attached pneumatic control units was installed onto an aluminum frame. (3) At the bottom of the acrylic plate, various powers supplies were installed, including LRS-50-5V10A for valve modules, RS-15-24V0.625 A for solenoid valves, and RS-15-5V3A for gateways (all from Mean-Well). Additionally, circuit boards and solenoid valves were also installed.

Testing. We designed a setup to evaluate the performance of the pneumatic control unit, as shown in Supplementary Fig. 7. The setup involved the following components and steps. A vacuum pump was connected to a barrel vacuum (T0702007, Fujiwara) to generate a vacuum source, and the pressure within the vacuum barrel was continuously monitored using an electrical pressure gauge (Fujiwara). Additionally, a mechanical valve was placed between the pressure gauge and the pneumatic control unit. Before testing, the mechanical valve was closed. The vacuum pump was then activated to supply a vacuum pressure of 80 kPa to the barrel vacuum. After achieving the desired vacuum pressure, the vacuum pump was turned off, and the mechanical valve was opened. We then proceeded to control the ON/OFF states of the pneumatic control unit. The pressure variations within the vacuum barrel were recorded.

Digital control

Client. We used Visual Studio development tools and C# language to design the client-side interface. In the client, the ON/OFF state of pneumatic control array was translated into a grayscale map. Then, the grayscale map data was then partitioned and organized into data packets. To ensure the integrity and accuracy of the data, a cyclic redundancy check (CRC) was performed on each data packet. Once the data packets were prepared and verified, they were transmitted to the data gateway module via WiFi.

Wireless communication gateway. The main structures of hardware circuit (Jialichuang) consist of a MCU chip (STC32G12K128, Hongjing), a WiFi module (E103-W03, Ebyte), a transceiver chip (TJA1050T, NXP) for CAN communication bus, a transceiver chip (MAX13487EESA, Maxim Integrated Products) for 485 communications bus, and a low dropout regulator chip (RS3236-3.3YF5, Texas Instruments). This module possesses a wireless access point (AP) mode, which ensures that the client has a direct wireless connection to the gateway. This module also has a wireless client mode, where the client connects to the gateway through the server relay mode, thus allowing remote-control operations from distant locations. After receiving the data packet sent by the client, the gateway first performs data verification to ensure accuracy and integrity. It then recognizes the identifiers within the data packet and routes the packet to the appropriate communication bus for further processing.

Solenoid valve module. The main components of hardware circuit consist of a MCU chip and a transceiver chip for 485 communication bus (Supplementary Fig. 6). The 485 communication bus received the data packet and processed the data packet to obtain control commands, which drive the MOSFET through the IO port of the MCU to amplify the actuation current. Then, the relay was triggered, and the state of the solenoid valve was switched.

Stepping motor module. The main components of hardware circuit consist of a MCU chip, a transceiver chip for 485 communication bus and a driver chip (DRV8825PWPR, Texas Instruments) for stepping motors (Supplementary Fig. 6). The 485 communication bus received the data packet, processed the data packet to obtain control commands, and drove the stepping motors.

Pneumatic control unit. The main components of hardware circuit consist of a MCU chip and a transceiver chip for CAN communication bus (Supplementary Fig. 6). After receiving the data packet sent by the data gateway, the data verification should be carried out to make sure the data is correct. Then, the data was processed as follows: Extracting the picture data (8 × 8) in the packet and then checking for the presence of any non-zero bytes in the first row. The existence of a non-zero byte indicates that the corresponding row requires actuation. After identifying the rows that need actuation, the specific positions of the non-zero bytes within these rows are determined. This step identifies the specific columns that require actuation. The identified data points are then transmitted to the pulse-width modulation (PWM)

drivers. These drivers are responsible for actuating the steering engines, thereby achieving precise pneumatic control for the first row. Following the completion of the first row, the system processes the remaining rows in a similar line-by-line manner.

Pneumatic control array. The 12 pneumatic control units were interconnected using a single CAN communication bus, and the communication rate can reach up to 1 Mbps. Each pneumatic control unit is assigned a unique ID, which serves as its communication address. According to the ID of the pneumatic control, the gateway sent the data packet to the CAN communication bus in a sequential manner.

Large-scale array fabrication

To enhance efficiency for larger-scale projects, such as a 32 × 24 array, we developed a customized dispensing machine for silicone adhesives (Sil-poxy, Smooth-On), as shown in Supplementary Fig. 8. This machine, equipped with a 5 ml syringe and nozzles of 1 mm diameter and 12 mm length, streamlines the process. The fabrication begins with casting top and bottom elastomeric strips, each containing grooves (half of an elastomeric pocket), from soft silicone elastomer (Ecoflex 00-30, Smooth-On) using 3D-printed molds. The dispensing machine then precisely extrudes silicone adhesives at the ends of these grooves on the bottom strips. Zigzag strips are interleaved into these grooves, and the machine applies silicone adhesives along the sides of the grooves. After positioning the air ducts, the assembly is covered with the top elastomeric strips, rapidly preparing the interleaved assemblies. The next phase involves preparing a stretchable substrate from soft silicone elastomer (Dragon Skin 20, Smooth-On) using 3D-printed molds. Silicone adhesives are extruded onto this substrate, and anchors are then attached. Further, the adhesive is applied to these anchors, and the interleaved assembly strips are pasted on, completing the fabrication. The final step involves fixing the stretchable substrate to a customized uniaxial stage on the valve device, readying the system for operation.

Transforming a color image into an operation matrix

We utilized Python 3.10 and its image processing libraries to convert a color image into a volumetric surface map, a process detailed in Supplementary Fig. 9. The first step involved reading the color image and extracting its RGB values using the Python Imaging Library (PIL), where the 'open' function in PIL loaded the image, and the RGB values of each pixel were accessed. These RGB values were then converted into grayscale by calculating a weighted sum of the R, G, and B values, with weights of 0.2989, 0.5870, and 0.1140, respectively, reflecting the perceived luminance in human vision. The grayscale values, ranging from 0 (black) to 255 (white), were subsequently translated into height values through a linear transformation, mapping 0 to a minimum height and 255 to a maximum height, thus creating a height map of the image. Using the analytical model, we calculated the residual pre-strain for each interleaved assembly corresponding to these height values, resulting in the operation matrix M. This matrix then guided the hardware control system, actuating the dynamic 3D surface to morph into the desired target structures.

Evaluation of dynamic 3D metasurface on visually impaired subjects

Participants. Our study involved 14 visually impaired participants (8 males, 6 females), ranging in age from 26 to 53 years (mean age: 37.9, standard deviation, sd: 7.3). We included individuals with a medically verified visual impairment who were capable of performing tactile recognition tasks. The study procedures received approval from the Westlake University's Ethical Review Board (approval number: 20230731JHQ001), and all participants provided informed consent.

Procedures and data collection. The user study consisted of two perception experiments and a questionnaire to assess subjective experiences. In Experiments 1 and 2, participants engaged in identifying five basic geometric shapes (square, ellipse, parallelogram, rectangle, triangle), each presented with two different buckling heights (5.6 mm and 8.1 mm) to simulate varied shapes, as shown in Fig. 7a. Participants were asked to report the shape they perceived, and the duration taken for each identification, termed 'time cost', was recorded. Each participant identified each shape once in both experiments. After these experiments, the participants completed a NASA-TLX questionnaire, which evaluated the psychological and workload aspects of using the device. This questionnaire included six dimensions: physical demand, mental demand, temporal demand, own performance, effort, and frustration.

Statistical analysis. Due to the non-normal distribution of the time cost data, we employed a non-parametric Paired-Samples Wilcoxon Test to analyze the differences in time cost across the five shapes at the two buckling heights. The results of this test are presented in Supplementary Tab. 1. Additionally, we used a non-parametric Kruskal-Wallis Test to assess differences in time cost among the shapes. A post-hoc analysis with the Dunn Test was conducted to further investigate the time cost differences identified by the Kruskal-Wallis test. The Dunn Test's chi-squared (χ^2) values supported the findings from the Kruskal-Wallis test, confirming the reliability of our results. To ensure the integrity of the error rate, *P*-values were adjusted using the Bonferroni method. Detailed statistical results can be found in Supplementary Tab. 1.

Reporting summary

Further information on research design is available in the Nature Portfolio Reporting Summary linked to this article.

Data availability

Source data are provided with this paper.

Code availability

The codes generated in this study have been deposited in the Figshare database, which is available at https://doi.org/10.6084/m9.figshare.26526916.

References

1. Li, G. et al. Self-powered soft robot in the Mariana Trench. *Nature* **591**, 66–71 (2021).
2. An, S. et al. A mechanically robust and facile shape morphing using tensile-induced buckling. *Sci. Adv.* **10**, eado8431 (2024).
3. Whitesides, G. M. Soft Robotics. *Angew. Chem. Int. Ed.* **57**, 4258–4273 (2018).
4. Babaee, S. et al. Kirigami-inspired stents for sustained local delivery of therapeutics. *Nat. Mater.* **20**, 1085–1092 (2021).
5. Babaee, S. et al. Bioinspired kirigami metasurfaces as assistive shoe grips. *Nat. Biomed. Eng.* **4**, 778–786 (2020).
6. Overvelde, J. T. B., Weaver, J. C., Hoberman, C. & Bertoldi, K. Rational design of reconfigurable prismatic architected materials. *Nature* **541**, 347–352 (2017).
7. Overvelde, J. T. B. et al. A three-dimensional actuated origami-inspired transformable metamaterial with multiple degrees of freedom. *Nat. Commun.* **7**, 10929 (2016).
8. Yang, T. H. et al. Recent Advances and Opportunities of Active Materials for Haptic Technologies in Virtual and Augmented Reality. *Adv. Func. Mater.* **31**, 2008831 (2021).
9. Leroy, E., Hinchet, R. & Shea, H. Multimode Hydraulically Amplified Electrostatic Actuators for Wearable Haptics. *Adv. Mater.* **32**, 2002564 (2020).

10. Aharoni, H., Xia, Y., Zhang, X., Kamien, R. D. & Yang, S. Universal inverse design of surfaces with thin nematic elastomer sheets. *Proc. Natl. Acad. Sci. USA* **115**, 7206–7211 (2018).
11. Dradrach, K. et al. Light-driven peristaltic pumping by an actuating splay-bend strip. *Nat. Commun.* **14**, 1877 (2023).
12. Ware, T. H., McConney, M. E., Wie, J. J., Tondiglia, V. P. & White, T. J. Voxelated liquid crystal elastomers. *Science* **347**, 982–984 (2015).
13. Hajiesmaili, E., Larson, N. M., Lewis, J. A. & Clarke, D. R. Programmed shape-morphing into complex target shapes using architected dielectric elastomer actuators. *Sci. Adv.* **8**, eabn9198 (2022).
14. Ji, X. et al. An autonomous untethered fast soft robotic insect driven by low-voltage dielectric elastomer actuators. *Sci. Robot.* **4**, eaaz6451 (2019).
15. Sydney Gladman, A., Matsumoto, E. A., Nuzzo, R. G., Mahadevan, L. & Lewis, J. A. Biomimetic 4D printing. *Nat. Mater.* **15**, 413–418 (2016).
16. Kim, J., Hanna, J. A., Byun, M., Santangelo, C. D. & Hayward, R. C. Designing Responsive Buckled Surfaces by Halftone Gel Lithography. *Science* **335**, 1201–1205 (2012).
17. Na, H. et al. Hydrogel-based strong and fast actuators by electro-osmotic turgor pressure. *Science* **376**, 301–307 (2022).
18. Hu, W., Lum, G. Z., Mastrangeli, M. & Sitti, M. Small-scale soft-bodied robot with multimodal locomotion. *Nature* **554**, 81–85 (2018).
19. Kim, Y., Yuk, H., Zhao, R., Chester, S. A. & Zhao, X. Printing ferromagnetic domains for untethered fast-transforming soft materials. *Nature* **558**, 274–279 (2018).
20. Choi, G. P., Dudte, L. H. & Mahadevan, L. Programming shape using kirigami tessellations. *Nat. Mater.* **18**, 999–1004 (2019).
21. Hong, Y. et al. Boundary curvature guided programmable shape-morphing kirigami sheets. *Nat. Commun.* **13**, 133119 (2022).
22. Dudte, L. H., Vouga, E., Tachi, T. & Mahadevan, L. Programming curvature using origami tessellations. *Nat. Mater.* **15**, 583–588 (2016).
23. Li, Y. & Yin, J. Metamorphosis of three-dimensional kirigami-inspired reconfigurable and reprogrammable architected matter. *Mater. Today Phys.* **21**, 100511 (2021).
24. Callens, S. J. & Zadpoor, A. A. From flat sheets to curved geometries: Origami and kirigami approaches. *Mater. Today* **21**, 241–264 (2018).
25. Siéfert, E., Reyssat, E., Bico, J. & Roman, B. Bio-inspired pneumatic shape-morphing elastomers. *Nat. Mater.* **18**, 24–28 (2018).
26. Jones, T. J., Jambon-Puillet, E., Marthelot, J. & Brun, P. T. Bubble casting soft robotics. *Nature* **599**, 229–233 (2021).
27. Morin, S. A. et al. Camouflage and display for soft machines. *Science* **337**, 828–832 (2012).
28. Gao, T., Bico, J. & Roman, B. Pneumatic cells toward absolute Gaussian morphing. *Science* **381**, 862–867 (2023).
29. Davidson, Z. S. et al. Monolithic shape-programmable dielectric liquid crystal elastomer actuators. *Sci. Adv.* **5**, eaay0855 (2019).
30. Hwang, D., Barron, E. J., Haque, A. B. M. T. & Bartlett, M. D. Shape morphing mechanical metamaterials through reversible plasticity. *Sci. Robot.* **7**, eabg2171 (2022).
31. Pikul, J. H. et al. Stretchable surfaces with programmable 3D texture morphing for synthetic camouflaging skins. *Science* **358**, 210–214 (2017).
32. Han, M. et al. Three-dimensional piezoelectric polymer microsystems for vibrational energy harvesting, robotic interfaces and biomedical implants. *Nat. Electron.* **2**, 26–35 (2019).
33. Xu, S. et al. Assembly of micro/nanomaterials into complex, three-dimensional architectures by compressive buckling. *Science* **347**, 154–159 (2015).
34. Khang, D.-Y., Jiang, H., Huang, Y. & Rogers, J. A. A Stretchable Form of Single-CrystalSilicon for High-PerformanceElectronics on Rubber Substrates. *Science* **311**, 208–212 (2006).
35. Kim, B. H. et al. Three-dimensional electronic microfliers inspired by wind-dispersed seeds. *Nature* **597**, 503–510 (2021).
36. Liu, K. F. H. C. & Daraio Robotic surfaces with reversible, spatio-temporal control for shape morphing and object manipulation. *Sci. Robot.* **6**, eabf5116 (2021).
37. Bai, Y. et al. A dynamically reprogrammable surface with self-evolving shape morphing. *Nature* **609**, 701–708 (2022).
38. Bai, K. et al. Geometrically reconfigurable 3D mesostructures and electromagnetic devices through a rational bottom-up design strategy. *Sci. Adv.* **6**, eabb7417 (2020).
39. Fu, H. et al. Morphable 3D mesostructures and microelectronic devices by multistable buckling mechanics. *Nat. Mater.* **17**, 268–276 (2018).
40. Johnson, B. K. et al. A multifunctional soft robotic shape display with high-speed actuation, sensing, and control. *Nat. Commun.* **14**, 4516 (2023).
41. Hajiesmaili, E. & Clarke, D. R. Reconfigurable shape-morphing dielectric elastomers using spatially varying electric fields. *Nat. Commun.* **10**, 183 (2019).
42. Zhang, M. et al. Hydrogel muscles powering reconfigurable micro-metastructures with wide-spectrum programmability. *Nat. Mater.* **22**, 1243–1252 (2023).
43. Steed, A., Ofek, E., Sinclair, M. & Gonzalez-Franco, M. A mechatronic shape display based on auxetic materials. *Nat. Commun.* **12**, 4758 (2021).
44. Ni, X. et al. Soft shape-programmable surfaces by fast electromagnetic actuation of liquid metal networks. *Nat. Commun.* **13**, 5576 (2022).
45. Cui, J. et al. Nanomagnetic encoding of shape-morphing micromachines. *Nature* **575**, 164–168 (2019).
46. Alarcón, H. et al. Self-Amplification of Solid Friction in Interleaved Assemblies. *Phys. Rev. Lett.* **116**, 015502 (2016).
47. Wang, Y., Li, L., Hofmann, D., Andrade, J. E. & Daraio, C. Structured fabrics with tunable mechanical properties. *Nature* **596**, 238–243 (2021).
48. Cheng, X. et al. Programming 3D curved mesosurfaces using microlattice designs. *Science* **379**, 1225–1232 (2023).
49. Han, M. et al. Submillimeter-scale multimaterial terrestrial robots. *Sci. Robot.* **7**, eabn0602 (2022).
50. Ni, C. et al. Shape memory polymer with programmable recovery onset. *Nature* **622**, 748–753 (2023).

Acknowledgements

We thank the Research Center for Industries of the Future (RCIF) at Westlake University and Westlake Education Foundation for supporting this work. This work was supported by the National Natural Science Foundations of China (Grants 12350003, H.J.). We thank Mr. Cheng Zhao for helping with human experiments.

Author contributions

S.A., X.L., Z.G., Y.H. and H.J. developed the concept. S.A., X.L., and Y.H. designed and prototyped the devices. Y.H. developed the control system and software. S.A., X.L., Z.G., Y.H. and H.J. carried out experiments and analysis. Z. G. collected and analyze the user data. S.A. and Y.Z. carried out mechanical modelling and simulation. S.A. and X.L. created the videos. S.A., X.L., Z.G., and H.J. wrote the manuscript. H.J. supervised the project.

Competing interests

The authors declare no competing interests.

Additional information

Supplementary information The online version contains supplementary material available at https://doi.org/10.1038/s41467-024-51865-x.

Correspondence and requests for materials should be addressed to Hanqing Jiang.

Peer review information *Nature Communications* thanks Xueju Wang, and the other, anonymous, reviewers for their contribution to the peer review of this work. A peer review file is available.